

# Assessment of numerical aspects using LES in particle separation devices

*J. Muela\**, *J. Rigola\**, *C. Oliet\**, *C.D. Pérez-Segarra\**, and *A. Oliva\*<sup>†</sup>*

*\*Termo Fluids S.L., Av. Jacquard 97-E, 08227, Terrassa (Barcelona), Spain.*

*\* Heat and Mass Transfer Technological Center (CTTC), Universitat Politècnica de Catalunya-BarcelonaTech(UPC), ESEIAAT, Colom 11, 08222, Terrassa (Barcelona), Spain.*

jordi.muela@termofluids.com · quim@cttc.upc.edu · carles@cttc.upc.edu · segarra@cttc.upc.edu · oliva@cttc.upc.edu

<sup>†</sup>Corresponding author

June 19, 2019

## Abstract

Numerical simulations can be a powerful tool for the design and optimization of Foreign Object Debris (FOD) protection and separation devices. This work aims to study the relevance and influence of different modelling and numerical aspects in simulations of FOD devices using Large Eddy Simulation (LES) modelling. The results show that in LES some numerical aspects can be critical and must be carefully considered aiming to obtain accurate and reliable results. It is presented how some models affect the physics of the phenomena involved in these kind of flows as well as their impact on the accuracy of the simulations.

## 1. Introduction

Nowadays, the aerospace industry is devoting many resources towards the development of the More Electrical Aircraft (MEA) concept, and ultimately the achievement of an All Electrical Aircraft (AEA). The aim of these MEAs is the optimization of the aircraft performance, decreasing its operational and maintaining costs as well as reducing the gas emissions. The main idea behind the MEA is the substitution and replacement of all non-propulsive systems fully or partially driven by hydraulic, pneumatic or mechanical power sources, by systems fully driven by electric power.<sup>25</sup>

One of these systems is the Environment Control System (ECS), which controls the temperature, pressure and air flow into the aircraft. Conventionally, the inlet fresh air required for feeding the compressors of the ECS is obtained by bleeding high pressure, high temperature air from the latter stages of the compressors of the main aircraft engines or from the Auxiliary Power Unit (APU). This operational way guarantees the supply of a clean air without FOD to ECS compressors. These compressors operate at high rotational speed and have tight tolerances, and hence, the turbo-compressors may suffer a severe damage if FOD is ingested. However, this bleeding induces an additional fuel burn and lead to the ingestion of potential harmful neurotoxic substances found in engine oil.<sup>28</sup>

In order to overcome these issues, new Electrical Environment Control System (eECS) are being investigated and developed. These eECS do not bleed air from the engine, but they are feed with air coming directly from the ambient atmosphere via an intake mounted to the fuselage. Although this new concept overcomes the problems of the former ECS, drawing the fresh air directly from the ambient adds a new problematic, since now the system does not possess the protection against FOD guaranteed by the turbo fan and compressor of a commercial aircraft. Therefore, a protection system against this FOD should be employed before the turbo compressor of the eECS in order to minimize the risk of possible ingestion for all kind of FOD. Thus, the development of an efficient and reliable FOD protection system is a key and crucial aspect for the successful implementation of eECS on commercial aircrafts. Two possible candidates to be part of this FOD protection system are the Vortex Tube Separators and the Inertial Particle Separators (IPS).<sup>9</sup> The aim when designing these devices must be achieve enough FOD protection and the minimum pressure loss.

Computational Fluid Dynamic (CFD) simulations may become a powerful and helpful tool for the successful design and implementation of these devices in modern commercial aircrafts. Nonetheless, the employment of CFD on these configurations is not straightforward since many modelling uncertainties may arise (i.e. which forces are relevant, which is the influence of particle-wall and inter-particle collisions, turbulence modelling, etc.). Hence, the present work aims to shed some lights about the influence of these modelling issues. In order to do these studies, a benchmark case in a relatively simple canonical geometry with a flow pattern similar to the one found at IPS devices

## ASSESSMENT OF NUMERICAL ASPECTS USING LES IN PS DEVICES

has been selected. The case chosen is the experiment carried out by Kliafas and Holt.<sup>16</sup> This experiment consists in an air-solid two-phase flow in a squared duct with a 90° vertical-to-horizontal bend. Then, several simulations have been done reproducing the selected experiment and analysing the influence of different modelling and numerical aspects on the simulations results.

The paper is organized as follows. First, in Section 2 is detailed the mathematical description of dispersed multi-phase turbulent flows using a Eulerian-Lagrangian (EL) approach in LES modelling. Then, in Section 3 the configuration of the reproduced experiment is briefly described. Moreover, it is also detailed the numerical set-up employed to carry out the simulations. Next, in Section 4, the results obtained for the different models and numerical aspects analysed in this work are presented. The results obtained for each one of the aspects addressed are examined and studied in detail individually at separate subsections. Finally, conclusions and future work are discussed in Section 5.

## 2. Mathematical model

Simulations of dispersed multiphase flows involves the resolution of both continuous and dispersed phases. Among the different numerical methods available to simulate this kind of flows,<sup>10</sup> in the present work the EL approach has been employed.<sup>31</sup> It is based on a point-particle approach, where particles or groups of identical particles, known as parcels, are tracked individually throughout all the computational domain. Hence, in this method the dispersed phase is represented employing a Lagrangian reference framework, while the continuous phase is solved using the classical Eulerian frame. Moreover, the continuous phase is solved under the framework of LES modelling. Although LES is computationally more expensive than Reynolds Averaged Navier-Stokes (RANS) approach, it allows capturing the unsteadiness and complexity of the flow patterns characterizing these devices, which can be very relevant on the dispersed phase motion. Following, the governing equations describing both continuous and dispersed phases are detailed.

### 2.1 Continuous phase

The governing equations describing the behaviour of the continuous phase are the Navier-Stokes (NS) equations. In LES modelling, the large scales of the flow are solved, while the subgrid-scales (SGS) are modelled. This scale separation is obtained applying a low-pass filter to the transport equations.<sup>23</sup> For incompressible flows with constant viscosity, the filtered NS equations are:

$$\nabla \cdot \bar{\mathbf{u}} = 0 \quad (1)$$

$$\frac{\partial \bar{\mathbf{u}}}{\partial t} + \nabla \cdot (\bar{\mathbf{u}}\bar{\mathbf{u}}) = -\frac{1}{\rho} \nabla \bar{p} + \nu \nabla^2 \bar{\mathbf{u}} - \nabla \cdot \boldsymbol{\tau}^R + \mathbf{g} \quad (2)$$

where  $t$  represents time,  $\rho$  is the density,  $\mathbf{u}$  is the velocity vector,  $p$  stands for the pressure,  $\mathbf{g}$  the gravity and  $\boldsymbol{\tau}^R$  is the residual (or sub-grid) stress tensor. This last term must be modelled in order to close Eq. (2). In the present work this term is closed by means of an eddy-viscosity-type model following the Boussinesq hypothesis.<sup>24</sup>

### 2.2 Dispersed phase

As aforementioned, the dispersed phase is modelled employing a Lagrangian reference framework. The motion of particles and droplets in a fluid using a Lagrangian framework can be described by classical equations of motion, i.e., Newton's law. The first authors to work and develop a model for the dispersed phase using this approach were Basset,<sup>2</sup> Boussinesq<sup>3</sup> and Oseen.<sup>21</sup> Hence, the equation of motion for particles derived from their work is known as the **BBO-equation**. This BBO-equation was extended to non-uniform flow for small rigid particles by Maxey and Riley.<sup>18</sup> In general, the ordinary differential equations required to describe the behaviour of the dispersed phase are:

$$\frac{d\mathbf{x}_p}{dt} = \mathbf{v}_p \quad (3)$$

$$m_p \frac{d\mathbf{v}_p}{dt} = \sum_i \mathbf{F}_i \quad (4)$$

where  $m_p$  is the particle mass,  $\mathbf{v}_p$  the particle velocity,  $\mathbf{x}_p$  is the particle's position and  $\sum_i \mathbf{F}_i$  is the sum of all the relevant forces acting over the particle.

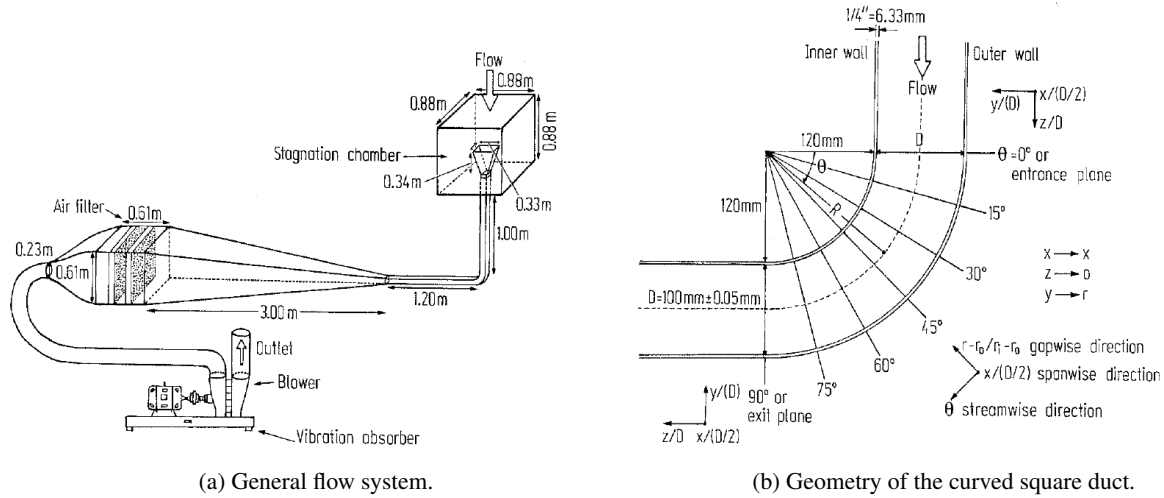


Figure 1: Experimental set-up of the experiment carried out by Kliafas and Holt.<sup>16</sup>

Particle-wall collisions are a very relevant phenomena in confined two-phase flows. Therefore, when studying IPS devices using numerical simulations, it is required to use a model capable to correctly predict the physics of particle-wall collision events. An ideal approach is to consider all the collisions as elastic and that all the surfaces are ideally smooth. This approach preserves the kinetic energy of the particles after the collision against the wall and considers that the surfaces are ideal and do not have roughness. Nonetheless, in reality, the surfaces have a certain roughness and the collisions of the particles against the walls are inelastic. Therefore, in order to correctly predict particle-wall collisions it is required to properly model surface roughness and the inelastic collisions. In the present work, the particle-wall model presented by Breuer et al.<sup>4</sup> has been employed. In this model, the roughness of the surfaces is modelled by means of the Sandgrain roughness model. This model assumes that the surface is covered by a “bed” of spherical sand grains mono-sized and perfectly packed. Hence, the surface roughness is modelled through the radius of these mono-sized sand grains. Regarding the inelastic collision, it is modelled employing an inelastic hard sphere collision model including friction.<sup>4,6</sup> This model requires the normal ( $e_n$ ) and tangential ( $e_t$ ) restitution coefficients, as well as both static ( $\mu_{st}$ ) and dynamic ( $\mu_{dy}$ ) friction coefficients. These values are dependant on the material of both particles and walls and they are typically not constant, varying in function of the impact angle and velocity. Therefore, a proper estimation of these values is required in order to correctly model the inelastic particle-wall collisions in the case of study.

### 3. Test case description

The reference benchmark case selected in order to carry out the present work is the experiment presented by Kliafas and Holt.<sup>16</sup> The experiment consisted in a 90° vertical-to-horizontal bend and two straight ducts of square cross-section (see Fig. 1). The vertical pipe before the bend has a length of  $L_v = 1$  m and the horizontal section downstream the bend is of  $L_h = 1.2$  m. The length of the cross-section is  $L_c = 100$  mm and the bend mean radius of curvature is  $R = 176$  mm.

At the inlet of the vertical section, a uniform steady flow with velocity  $U_b$  is obtained using a fine mesh screen. Regarding the dispersed phase, it consist in glass spheres of density  $\rho_p = 2990$  kg m<sup>-3</sup>. Two classes of particles with different diameters were employed,  $d_p = 50$   $\mu$ m and  $d_p = 100$   $\mu$ m. The particles are injected uniformly in the test section at the inlet of the vertical pipe with a mass flow rate of  $\dot{m}_p = 3.6$  g min<sup>-1</sup>. Two different inlet velocities were considered in the experiment, a low-speed case with  $U_b = 33.09$  m s<sup>-1</sup> ( $Re = 2.2 \times 10^5$ ) and a high-speed case with  $U_b = 52.19$  m s<sup>-1</sup> ( $Re = 3.47 \times 10^5$ ). In the present work, the high-speed case has been selected. For this one, only particles with  $d_p = 50$   $\mu$ m were injected. In this set-up, considering as characteristic length the side of the square pipe  $L_c$ , the particles have a Stokes number of  $St = 12.04$ .

The mean and radial velocity profiles for both continuous and dispersed phases were measured at 7 stations placed at the bend each 15°, starting at the entrance plane of the bend (0°) till the exit plane (90°), as depicted in Fig. 1b. The velocity profiles are given in the normalized radial coordinate  $r^* = (r - r_o) / (r_i - r_o)$ , where  $r_i$  and  $r_o$  are, respectively, the inner and outer wall radius of curvature.

### 3.1 Numerical set-up

All the numerical experiments performed in this work have been carried out using the in-house CFD software TermoFluids,<sup>17</sup> based on the finite volume method (FVM). This CFD code is parallel, highly scalable and designed to work in both structured and unstructured meshes.

The convective operator of the momentum equation (Eq. (2)) is discretized employing a second order Symmetry-Preserving (SP) scheme.<sup>33</sup> This discretization scheme constructs an anti-symmetric discrete convective operator. This operator does not introduce artificial dissipation in the momentum equation, and therefore the kinetic-energy is preserved. The diffusive operator is discretized by means of a second-order Central Differencing Scheme (CDS). Both convective and diffusive operators are integrated explicitly by means of a one-leg second-order time-integration scheme.<sup>32</sup> This scheme includes a free-parameter allowing to adapt its stability region. The free-parameter is dynamically selected maximizing the stability region in function of the eigenvalues of the discrete operators. Moreover, this time-integration strategy also selects the optimal time-step at each iteration. The pressure-velocity coupling is solved by means of the Fractional Step projection method.<sup>14</sup> The idea behind this technique is to split the momentum in two steps, with a first explicit step where an intermediate velocity  $\hat{\mathbf{u}}$  is obtained, followed by a second step where the pressure is solved implicitly and the intermediate velocity is corrected obtaining the physical velocity. The Poisson equation is solved by means of the iterative Conjugate-Gradient (CG) method with Jacobi diagonal scaling.

Regarding the dispersed phase, it is integrated employing a first-order semi-implicit time-integration scheme, where the terms depending on  $\phi^{n+1}$  are linearised. During the dispersed phase integration the continuous phase is considered *frozen*, and each particle is integrated in one or more  $i$  sub-time steps with a time-step of  $\Delta t_{p,i}$ . The particle is integrated  $n_p$  times until the time-step of the continuous phase is reached, i.e.,  $\Delta t = \sum_{i=1}^{n_p} \Delta t_{p,i}$ . The particle integration time-step  $\Delta t_{p,i}$  of each  $i$  step is selected as the minimum between the time-step of the continuous phase, the *particle response time*  $\tau_p$  or the travel time-step of the particle from its position and the first face crossed by the particle in its trajectory  $\Delta t_{i2f}$ , i.e.,  $\Delta t_{p,i} = \min(\Delta t, \tau_p, \Delta t_{i2f})$ . At each sub-integration step  $i$  the properties of the continuous phase are interpolated in the particles' position. Since TermoFluids is designed to work with unstructured meshes, interpolation methods for scattered data in multi-dimensions are employed.

## 4. Results

In this section are presented the results obtained for the different modelling and numerical aspects analysed in the present work. Each one of them is studied individually and reported in a different subsection. Each study assess the relevance of the analysed aspect and which is its impact over particles' motion.

### 4.1 Turbulence model

As aforementioned in Section 2.1, the term  $\tau^R$  appearing in Eq. (2) must be closed by means of a turbulence model. In the present work, three different turbulence models have been tested. The first one is the model proposed by Smagorinsky,<sup>29</sup> based on the Prandtl mixing length applied to SGS modelling. In this model the turbulent viscosity is proportional to the strain. The second one is the Wall-adapting eddy viscosity model (WALE) SGS model developed by Nicoud.<sup>20</sup> This model is based on the square of the velocity gradient tensor. The SGS viscosity obtained with this model takes into account the strain and the rotation rate of the smallest resolved turbulent fluctuations. Some features of this model are its capability of switching off in two-dimensional flows, in laminar flows, and when the length-scale is in the range of  $Re^{-3/4}$ . It also has a cubic behaviour near walls with respect to the normal direction of the wall. The last model studied is the variational multiscale (VMS) approach applied to the WALE. This method was originally formulated for the Smagorinsky model by Hughes.<sup>13</sup> Using this framework the modelling is confined to the effect of a small-scale Reynolds stress, in contrast with classical LES in which the entire SGS stress is modelled. Three simulations employing the **Mesh A** (later detailed in Section 4.2) and a uniform  $U_{bulk}$  velocity at the inlet have been carried out. The results obtained for the mean streamwise velocity of the continuous phase are depicted in Fig. 2.

As can be seen, the Smagorinsky model is very dissipative close to the walls, generating a very large boundary layer. On the other hand, both WALE and VMS models present very similar results. Both models are able to properly model the flow close to the walls. This aspect is crucial when simulating confined flows, like the one studied in the present work. Therefore, hereinafter the turbulence model employed in the following studies is the WALE model.

### 4.2 Mesh

Once selected the turbulence model, the following aspect addressed is the mesh. Due to the simplicity of the geometry, structured meshes have been employed (see Fig. 3). Different meshes have been generated varying the number of nodes

## ASSESSMENT OF NUMERICAL ASPECTS USING LES IN PS DEVICES

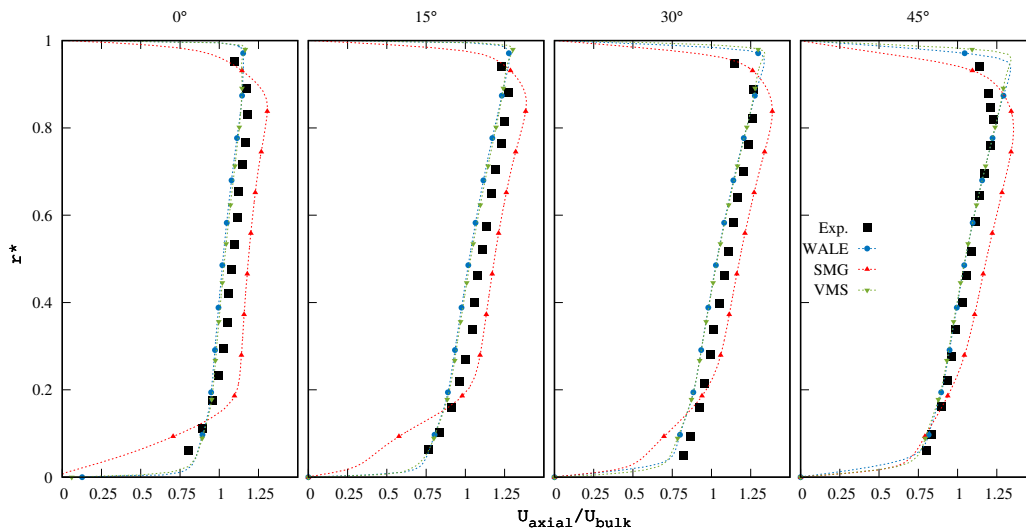


Figure 2: Mean streamwise velocity of the continuous phase for different turbulence models in Mesh A.

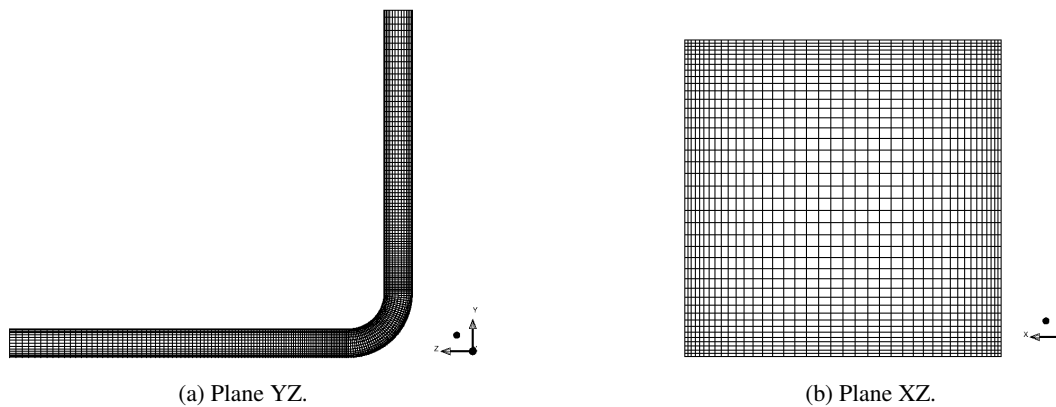


Figure 3: Mesh of the computational domain.

in the side of the cross-section, both vertical and horizontal ducts, and the bend. In the cross-section the mesh is refined close to the walls. In the bend, the control volumes (CVs) are spatially uniform. The first CV close to the bend of both vertical and horizontal ducts has the same size than the CVs of the bend. The generated meshes are detailed in Table 1. In this table is specified the number of CVs defined in each section. The value detailed in the column labelled as  $\Delta y$  is the height of the CV next to the wall, in the normal direction to it.

The study has been carried out for five different mesh (see Table 1). As in the previous study, a uniform flat velocity with value  $U_{bulk}$  has been imposed in the inlet section. The results obtained for the mean velocity in the first four stations are shown in Fig. 4. As can be seen, the mean streamwise velocity profiles obtained for the five different meshes are fairly similar in all the cases. The most significant differences are found in the boundary layer close to the walls. The finest mesh, Mesh E, captures a thinner boundary layer, especially downstream. On the other hand, the boundary layer obtained with the coarsest mesh, Mesh A, is the widest. The  $y^+$  obtained with the finest mesh is around  $\sim 1$ , so the boundary layer is being fully resolved. The results for the three intermediate meshes (B, C and D) are very similar. Therefore, as a compromise between accuracy and computational requirements, the **Mesh C** has been employed in all the following studies, if not specified otherwise.

A second comparison including particles has been carried out in this section. In this case, only meshes A and C have been compared. For these simulations, a turbulent velocity profile has been employed in the inlet section (see Section 4.3). Regarding the dispersed phase, the particle-wall collision has been modelled as elastic. The results of this comparison are depicted in Fig. 5. The obtained velocity profiles of the continuous phase are indicated with (f) while the results of the dispersed phase are designated with (p). Both meshes are able to retrieve good results for both continuous and dispersed phases, since the mean velocity profiles obtained in the simulations agree well with the ones of the experiment. As in the previous comparison, only minor differences are appreciated. Hence, it can be stated

## ASSESSMENT OF NUMERICAL ASPECTS USING LES IN PS DEVICES

Table 1: Meshes details.

Mesh	Square side	$\Delta y$	Vertical	Bend	Horizontal	Total CVs
A	50	0.50	150	100	160	<b>1.03M</b>
B	90	0.20	200	190	200	<b>4.78M</b>
C	64	0.25	380	143	300	<b>3.37M</b>
D	90	0.20	380	190	300	<b>7.05M</b>
E	120	0.02	380	190	300	<b>12.53M</b>

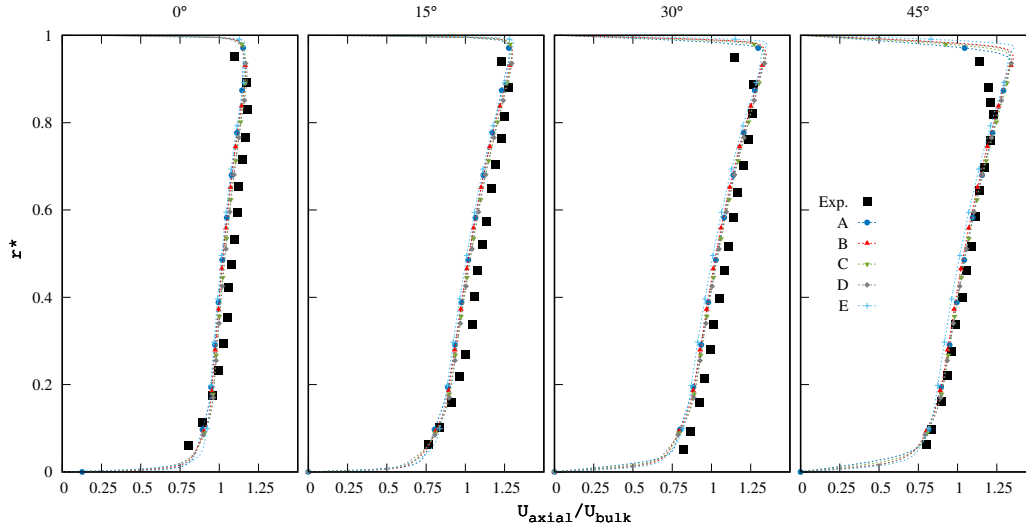


Figure 4: Results comparison for the continuous phase in the different meshes (inlet BC: flat profile).

that both meshes are capable of predict good results. Nonetheless, as indicated before, the more fine Mesh C has been retained for the following studies. Although it can be stated that the coarsest Mesh A is enough to obtain good results, it is preferred to employ a more fine mesh in other to carry out the following studies.

### 4.3 Inlet boundary conditions

The boundary conditions (BC) are a very relevant aspect in numerical simulations when reproducing experiments. However, sometimes is difficult to exactly reproduce the BCs of the experiment, specially at the inlet. Some experiments do not measure the real conditions at the inlet and just gives the supposed BC. Other experiments do measurements at the inlet but do not provide all the data required to reproduce the same flow conditions (e.g. only give first statistics). As seen in Sections 4.1 and 4.2, the obtained numerical results using a flat uniform velocity profile in the inlet give a mean velocity profile slightly different to the one reported in the experiments. The mean velocity seems underestimated at the inner region, while slightly overestimated close to the walls. Hence, it is suspected that although the authors of the experiment states that at the inlet of the vertical pipe (outlet of the contraction, see Fig. 1a) there is a flat uniform velocity, this is not completely true. Probably, the velocity profile was not perfectly flat and presented some turbulence level after the mesh screen at the inlet. In order to analyse the influence of the velocity profile at the inlet different options have been compared: i) flat velocity profile; ii) turbulent velocity profile obtained from an auxiliary simulation; iii) laminar velocity profile for square ducts presented by Purday<sup>27</sup> as an approximation of the analytical solution; iv) turbulent velocity profile generated using a synthetic turbulence generator presented by Klein.<sup>15</sup>

In order to generate the turbulent velocity profile an auxiliary simulation of a square duct with periodic boundary condition in the stream-wise direction have been employed. The velocity field generated at the mid-plane of the square duct is saved and later injected in the simulated domain at the inlet section. The laminar velocity profile for square ducts proposed by Purday<sup>27</sup> is defined by the function:

$$\frac{U}{U_{max}} = \left[ 1 - \left( \frac{y}{b} \right)^{m1} \right] \left[ 1 - \left( \frac{z}{a} \right)^{m2} \right] \quad (5)$$

where both values  $a$  and  $b$  are the same in a square duct and set as the value of side length of the cross-section, i.e.  $a = b = L_v$ . In this study both exponents  $m1$  and  $m2$  are defined with the same value, i.e.  $m = m1 = m2$ . Two

## ASSESSMENT OF NUMERICAL ASPECTS USING LES IN PS DEVICES

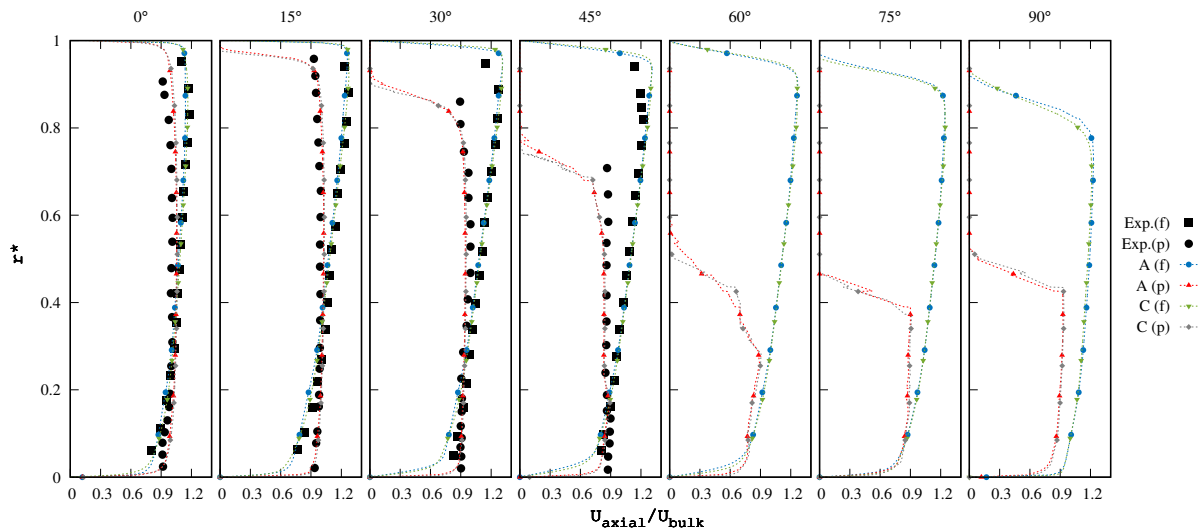


Figure 5: Results for continuous and dispersed phases comparing meshes A and C (inlet BC: turbulent).

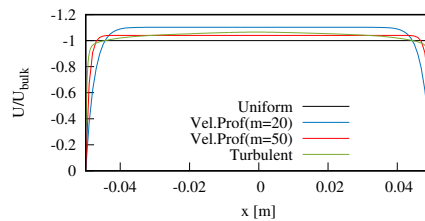


Figure 6: Inlet velocity profiles.

different values for the exponent  $m$  are tested,  $m = 20$  and  $m = 50$ . Regarding the synthetic turbulent method, it has been generated a turbulent velocity field using as velocity profile the Eq. (5) with  $m = 50$  and a turbulence intensity of 5%. A comparison of the proposed mean velocity profiles at the inlet is shown in Fig. 6.

The results obtained for the different BCs are depicted in Fig. 7. As can be seen, the results for the laminar velocity profiles and the turbulent profiles agree better with the experimental results than the flat velocity profile. Observing the inlet velocity profiles shown in Fig. 6, it can be seen that there is clear connection between the velocity profile imposed at the inlet and the mean velocity profiles obtained at the analysed stations of the bend. The laminar velocity profile with  $m = 20$ , the one with a bigger  $U_{max}$ , is the one giving a higher mean velocity at the centre in all the stations. On the other hand, the laminar profile with  $m = 50$ , which has a smaller  $U_{max}$  than the turbulent inlet, gives a mean velocity at the centreline lower than the turbulent inlet. Comparing the laminar velocity profile with exponent  $m = 50$  and the one generated with the synthetic turbulent method (both cases have the same mean velocity profiles), the obtained results are practically identical. Hence, it means that the turbulence in the inlet does not affect the results downstream for the first order statistics, at least with the turbulence intensity employed in this study.

In the experimental set-up described by Kliafas and Holt<sup>16</sup> is stated that a “uniform steady flow was obtained at the outlet of the contraction”, i.e. at the inlet of the vertical pipe. Nonetheless, the results shown in Fig. 7 seem to suggest that the velocity profile at the inlet was not a flat profile. In the experiment, no measurements were carried out at this section. Therefore, it is an uncertainty which was the real velocity profile at the inlet of the vertical pipe. Thus, based on the results obtained in this study, the turbulent velocity profile has been selected to carry out the subsequent analyses.

#### 4.4 Modelled forces

When simulating dispersed multi-phase flows, the importance of each one of the forces acting over the dispersed phase depends on the flow characteristics. Usually, the most relevant force acting over the dispersed phase is the drag force. Nonetheless, there are other forces (e.g., pressure gradient force, added mass force, Basset force, Saffman and Magnus lift forces, body forces, etc.) and effects like rarefaction, compressibility and Brownian motion that can be very relevant for the particle’s motion.<sup>6,10</sup>

## ASSESSMENT OF NUMERICAL ASPECTS USING LES IN PS DEVICES

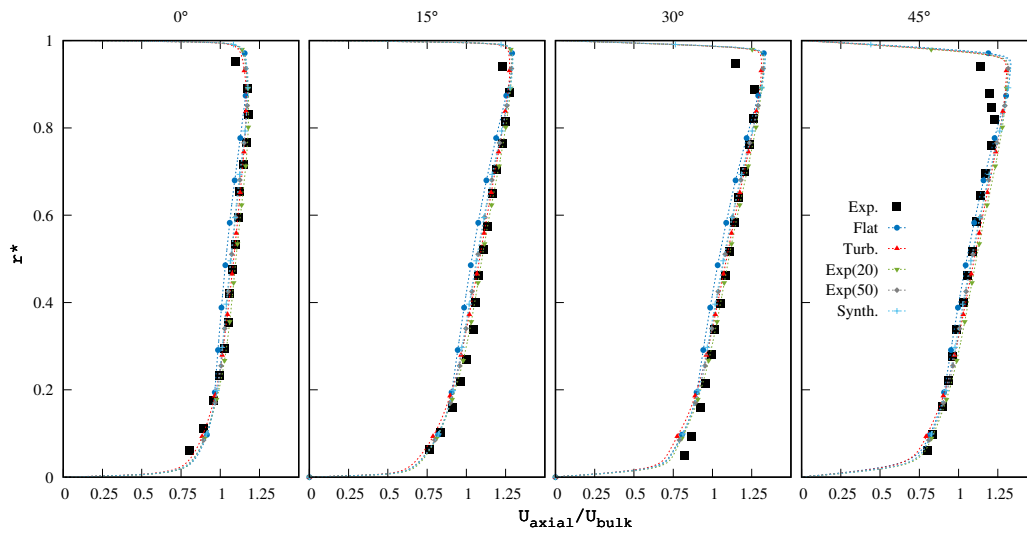


Figure 7: Results for the different inlet boundary conditions in mesh C.

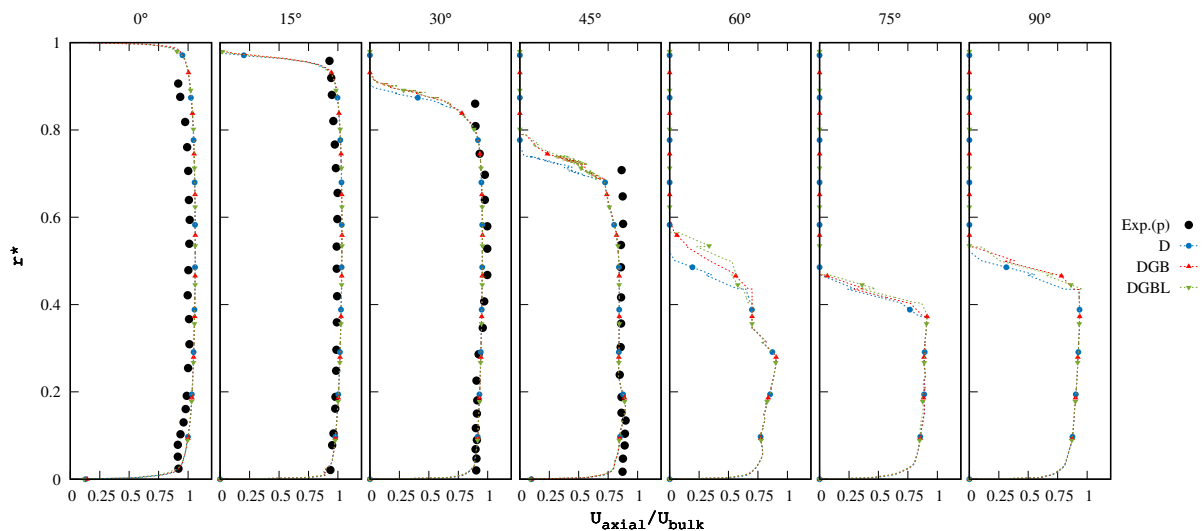


Figure 8: Results of the dispersed phase accounting for different forces affecting the particles.

In the present work has been analysed the influence of different forces on particles' motion in the studied configuration. Specifically, the studied forces have been: drag force, gravity, buoyancy and the Saffman lift force. The latter is a force experienced by particles moving in a shear layer. When travelling in a shear layer, the particles experience a non-uniform relative-velocity and hence, a non-uniform pressure distribution. This non-uniform pressure distribution originates a lift force acting in the direction of the higher slip velocity, i.e. if the particle has a lower velocity than the flow the lift force moves the particle away from the wall, while if the particle travels at a speed higher than the flow, Saffman lift acts pointing towards the wall. The correlation employed in order to take into account the Saffman lift force is the one proposed by Mei.<sup>19</sup> Regarding the drag force, the correlation used in the present work is the one given by Schiller and Naumann.<sup>26</sup>

Three different simulations have been carried out in order to analyse the relevance of the studied forces: a first one where only the drag force has been employed (D), a second one adding the gravity and the buoyancy (DGB), and a third one also including the Saffman lift force (DGBL). All the simulations have been done assuming an elastic boundary collision between the particles and the walls. The obtained results are depicted in Fig. 8. It can be noticed that for the studied case, the only relevant force is the drag force. No significant differences in the results were observed when the other forces were included. Therefore, in the following studies only the drag force has been retained.

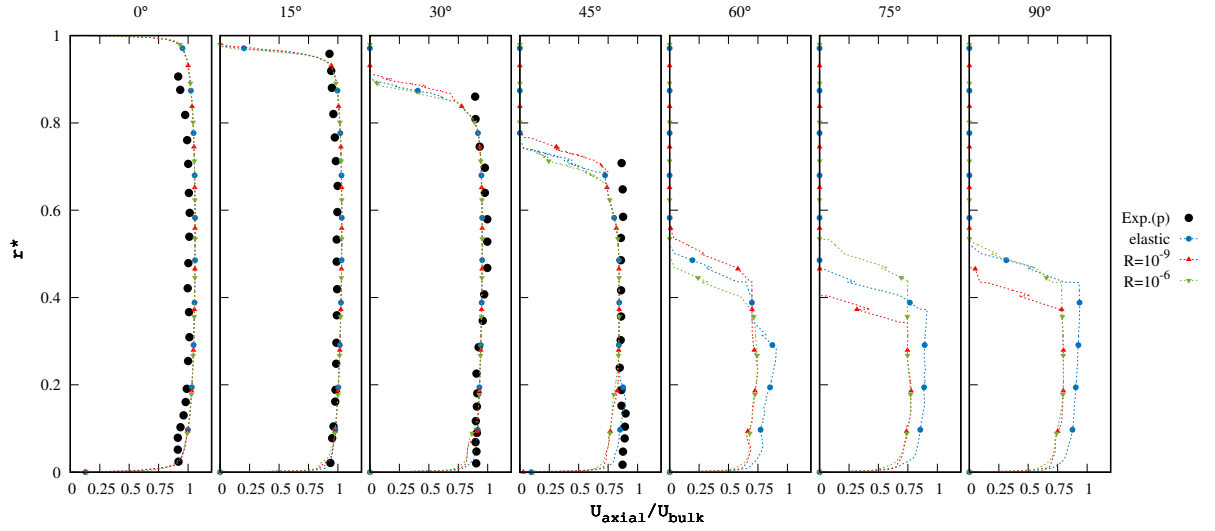


Figure 9: Results comparing elastic vs. inelastic collision modelling for particle-wall collisions.

#### 4.5 Elastic/inelastic collision

Another key aspect for the study of IPS devices is the modelling of the particle-wall collision physics. So far, in the previous studies the particle-wall collisions have been considered perfectly elastic. In this section is analysed the influence of modelling the collisions as inelastic and accounting for the roughness of the walls. The inelastic collisions are modelled employing the hard sphere collision model.<sup>6</sup> The effect of the surface roughness is included by means of the Sandgrain roughness model.<sup>4</sup> In this study, the behaviour of the particles in a case assuming perfectly smooth surfaces and elastic collisions has been compared against two cases modelling the particle-wall collisions as inelastic and supposing that the the surfaces have a certain roughness. The analysed roughness have been  $R = 1 \times 10^{-6}$  and  $R = 1 \times 10^{-9}$ . As commented in Section 2.2, the hard sphere collision model requires the normal ( $e_n$ ) and tangential ( $e_t$ ) restitution coefficients, as well as the static ( $\mu_{st}$ ) and dynamic ( $\mu_{dy}$ ) friction coefficients. In the present study these values have been calculated employing the model proposed by Sommerfeld and Huber,<sup>30</sup> where:

$$e_n(\alpha) = \max(1 + m_e \alpha, e_h) \quad (6)$$

$$e_t(\alpha) = 1 \quad (7)$$

$$\mu_{st}(\alpha) = \mu_{dy}(\alpha) = \max(\mu_0 + m_\mu \alpha, \mu_h) \quad (8)$$

where  $\alpha$  is the impact angle and the slopes are calculated as  $m_e = e_h - 1 / \alpha_e$  and  $m_\mu = \mu_h - \mu_0 / \alpha_{mu}$ . The values of the parameters appearing in Eqs. (6) to (8) are function of the pairing particle and wall materials. In this case the values for particles of glass and walls of plexiglass have been selected, i.e.,  $e_h = 0.73$ ,  $\alpha_e = 18$ ,  $\mu_0 = 0.4$ ,  $\alpha_\mu = 27$  and  $\mu_h = 0.15$ . In later sections it will be further analysed which is the impact of these parameters in the particle-wall collision events.

The results comparing the case assuming elastic collisions and the two others modelling the particle-wall collisions as inelastic and assuming surface roughness are shown in Fig. 9. From station  $30^\circ$  and downstream can be clearly appreciated the difference in the results. When considering inelastic collisions, the kinetic energy of the particles is reduced after the collisions against the wall. At stations  $30^\circ$  and  $45^\circ$  is appreciated how below the normalized radial coordinate  $r^* < 0.1$  and  $r^* < 0.2$ , respectively, the velocity of the particles that have experienced collisions is smaller when considering inelastic collisions. Comparing the simulation results with the experimental ones the elastic collision model seems to agree better. That means that although in real life collisions are inelastic, the restitution and friction coefficients employed do not model correctly the pairing materials of the experiment. The values employed in this comparison seem to overestimate the dissipation of the particles' kinetic energy after the collisions. Regarding the surface roughness, it seems to have an effect at station  $60^\circ$  and downstream. Depending on the roughness, the particles reach a different height after their collisions. Nonetheless, not only the roughness affects which is the height reached by the particles after their collision against the bend, but also the inelastic collision model has an effect. At stations  $75^\circ$  and  $90^\circ$ , the height for the lowest level of roughness ( $R = 1 \times 10^{-9}$ ), which is a very smooth surface, is below the elastic case. Since the kinetic energy of the particles is reduced after the collision, the particles are not able to reach neither the height nor the velocity of the elastic case. On the other hand, for the case with roughness  $R = 1 \times 10^{-6}$ ,

## ASSESSMENT OF NUMERICAL ASPECTS USING LES IN PS DEVICES

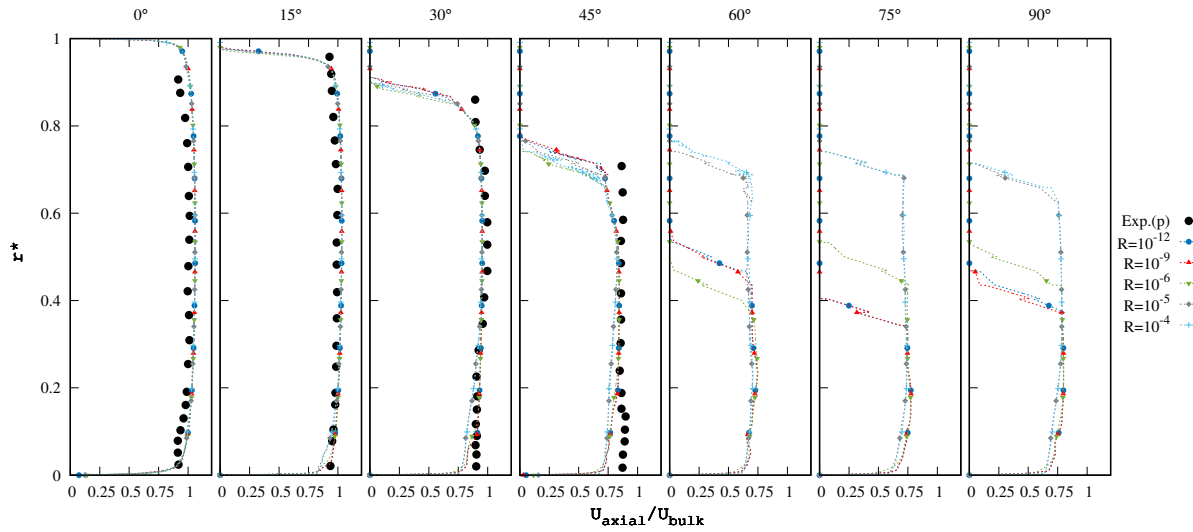


Figure 10: Results for the dispersed phase comparing different roughness.

although the particles suffer a reduction in their kinetic energy after collisions, the increment in the *randomness* of the particle direction after collision against walls produces an increase in the height reached for the particles in the later stations respect to the elastic case, even though with a smaller velocity. In the following subsection is further analysed the effect of the roughness on the particle-wall collision physics.

#### 4.6 Wall roughness

As aforementioned, in real-life applications the surfaces are not perfectly smooth, and depending on the material and the manufacturing process the surfaces present a characteristic roughness. This roughness can severely affect the particle-wall collision behaviour, and hence, should be correctly modelled. In this subsection is analysed the effect on the particles' trajectories for different roughness. In the Sandgrain roughness model<sup>4</sup> the surface roughness is modelled assuming that the surface is covered by a "bed" of grains perfectly spherical with a constant radius  $R$ . This radius  $R$  is related to classical values employed to characterise the surface roughness like the root-mean-squared roughness  $R_q$ . This relation is given by  $R = 0.5C_{surface}R_q$ , where  $C_{surface}$  is a constant depending on the surface material and the finishing process. Therefore, the higher the radius  $R$ , the more roughness. In this section five different roughness have been compared, ranging from a surface pretty smooth ( $R = 1 \times 10^{-12}$ ) up to a very rough surface ( $R = 1 \times 10^{-4}$ ).

The results for five different roughness are depicted in Fig. 10. Notice that in order to produce these results, the restitutions and friction coefficients are the ones previously employed in Section 4.5. At a first glance it can be seen a clear difference between the case with  $R \leq 1 \times 10^{-6}$  and the ones with  $R > 1 \times 10^{-6}$ . This threshold is related with the size of the studied particles ( $d_p = 100 \mu\text{m}$ ), since the bigger values of  $R$  model a grain spheres with a size in the order of magnitude with the size of the particles, severely affecting their trajectory after collisions. It can be seen that from station  $30^\circ$  and downwards, the regions with particles affected by collisions present a lower mean particle velocity for the cases with higher roughness. Apart from reducing the particle mean velocity, surfaces with a high roughness spread the particles in a wider angle after collision. This effect is clearly seen at station  $75^\circ$  and  $90^\circ$ , where the particles reach a higher height after colliding with the bend. This clear trend observed at the two last stations is not followed in the station  $60^\circ$ , where the height reached by the particles for case  $R = 1 \times 10^{-6}$  is the smallest one. In order to better understand why is this happening, it has been compared the mean volumetric fraction of four cases: one with elastic collisions, and three with inelastic collisions and the following roughness:  $R = 1 \times 10^{-5}$ ,  $R = 1 \times 10^{-6}$  and  $R = 1 \times 10^{-9}$ . In Fig. 11 is shown the isoline with a mean volumetric fraction of  $\alpha_{vf} = 1 \times 10^{-9}$ . It can be seen that at station  $60^\circ$  the case with  $R = 1 \times 10^{-6}$  presents a height below the elastic case and the one with  $R = 1 \times 10^{-9}$  is above. In this station, the particles setting the top height reached by the particles are the ones coming from close to the inner wall. Hence, probably they have collided very tangentially with the inner wall. For  $R = 1 \times 10^{-6}$ , particles after collision will have a trajectory less tangential to the inner wall than  $R = 1 \times 10^{-9}$ . This makes that the height at station  $60^\circ$  for case  $R = 1 \times 10^{-6}$  is below the one with  $R = 1 \times 10^{-9}$ . The reason why when considering inelastic collisions and  $R = 1 \times 10^{-9}$  the height at station  $60^\circ$  is higher than when considering elastic collisions is that this roughness is very small, almost negligible. This makes that the trajectory of the particles after collision with the inner wall is very similar to the elastic case. However, since the collision is inelastic, the particles lose kinetic energy, and are dragged

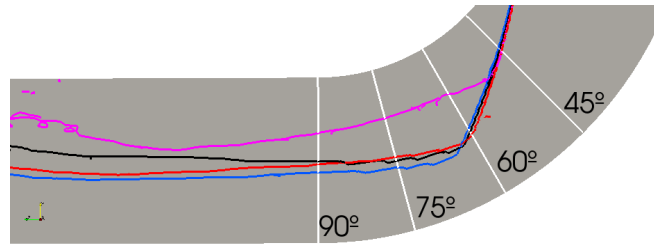


Figure 11: Isolines with mean volumetric fraction  $\alpha_{vf} = 1 \times 10^{-9}$  at mid-plane for cases: elastic (black),  $R = 1 \times 10^{-6}$  (red),  $R = 1 \times 10^{-9}$  (blue) and  $R = 1 \times 10^{-5}$  (pink).

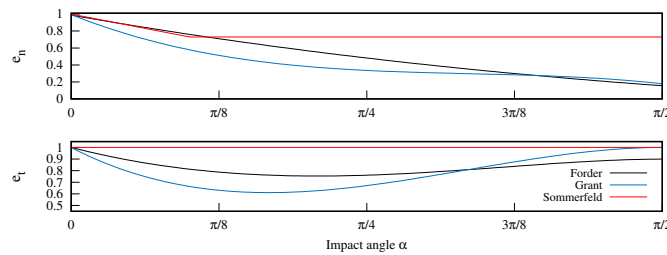


Figure 12: Values of the normal ( $e_n$ ) and tangential ( $e_t$ ) restitution coefficients.

more easily by the continuous phase. Since the flow at this station points to the outlet, the particles achieve a higher height than for the elastic case.

Another interesting aspect is that for the studied particle size, it seems that there is a certain roughness value  $R$  both above and below for which an increase or decrease in the degree of roughness do not change the particle-collision behaviour. Both roughness of  $R = 1 \times 10^{-5}$  and  $R = 1 \times 10^{-4}$  show very similar results, as well as the cases with  $R = 1 \times 10^{-9}$  and  $R = 1 \times 10^{-12}$ .

#### 4.7 Restitution coefficients

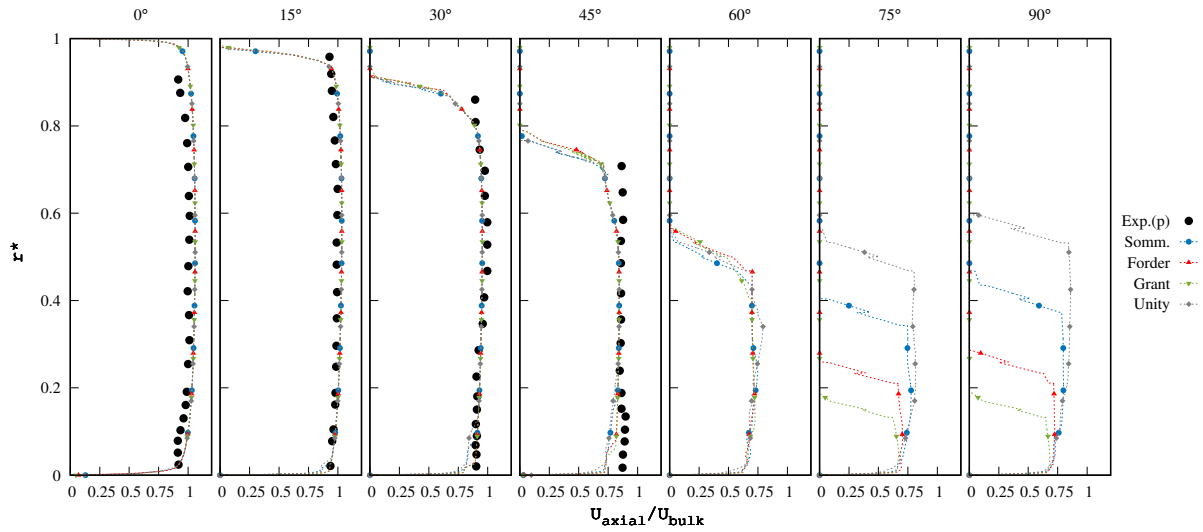
The next parameter analysed is the influence of both normal ( $e_n$ ) and tangential ( $e_t$ ) restitution coefficients. These coefficients relate the value of the normal and tangential velocities of the particle before and after the collision event against the wall. In order to study the influence of these parameters three different models for their evaluation have been compared: the one proposed by Forder et al.,<sup>11</sup> the model suggested by Grant and Tabakoff<sup>12</sup> and the model presented by Sommerfeld and Huber.<sup>30</sup> Moreover, a fourth case where  $e_n$  and  $e_t$  are assumed constant and equal to unity ( $e_n = e_t = 1$ ) has been analysed. The values for both coefficients given by the studied models as function of the impact angle  $\alpha$  are depicted in Fig. 12.

In Fig. 13 are compared the results obtained for the different models. As can be seen, the effect of these coefficients in the mean velocity of the particles after collision against the wall are very relevant. Taking a deeper look into the results, it can be observed a clear difference upstream and downstream the station  $60^\circ$ . At stations  $30^\circ$  and  $45^\circ$ , the region with collided particles show that the models of Forder and Grant seem to subtract less kinetic energy to the particles. On the other hand, at stations  $75^\circ$  and  $90^\circ$  the results show the opposite. This second behaviour is the one expected after looking the values returned by the models for both coefficients (see Fig. 12), where the Grant model should be the one reducing the most the particle mean velocity, followed by the one of Forder. On the other hand, the case done using ( $e_n = e_t = 1$ ) should be the one better preserving the kinetic energy of the particles, as it is observed in the two latter stations. Therefore, further studies must be carried out in order to fully understand the mechanisms that are causing the observed effects at stations  $30^\circ$  and  $45^\circ$ .

#### 4.8 Friction coefficients

In this subsection is studied the impact of the static ( $\mu_{st}$ ) and dynamic ( $\mu_{dy}$ ) friction coefficients. The value of the static friction coefficient will determine if a certain particle-wall collision event is *sliding* or *non-sliding*.<sup>4</sup> If the collision is of *sliding* type, then the Coulomb's law of friction is assumed to hold for the collision event and the dynamic friction coefficient must be taken into account. In order to carry out this study six different ways of calculating these coefficients have been analysed: one employing the correlation proposed by Sommerfeld and Huber<sup>30</sup> (see Eq. (8)) and

## ASSESSMENT OF NUMERICAL ASPECTS USING LES IN PS DEVICES

Figure 13: Results for different models employed to evaluate the normal ( $e_n$ ) and tangential ( $e_t$ ) restitution coefficients.

five cases where different constant values for both parameters are assumed. These combinations are summarized in Table 2.

Table 2: Studied combinations of static and dynamic friction coefficients.

$\mathbf{F}(\mu)$	$\mu_{st}$	$\mu_{dy}$
<b>Somm.</b> ( $\alpha$ )	$\max(\mu_0 + m_\mu \alpha, \mu_h)$	$\max(\mu_0 + m_\mu \alpha, \mu_h)$
<b>1</b>	0.14	0.14
<b>2</b>	0.4	0.4
<b>3</b>	0.7	0.7
<b>4</b>	1.0	1.0
<b>5</b>	1.0	0.4

The obtained results are shown in Fig. 14. As can be observed, the value of the friction coefficients has a big effect on the mean velocity of the particles after collision with the walls. Smaller values of the friction coefficients reduce to a lesser extent the kinetic energy of the particles, resulting in higher mean particle velocity after collisions. The cases *Somm.*( $\alpha$ ) and  $F(\mu) = 1$  give very similar results. For the correlation given by Eq. (8) the coefficients employed have been  $\mu_0 = 0.4$ ,  $\alpha_\mu = 27$  and  $\mu_h = 0.15$ , which means that for impact angles higher than  $27^\circ$  the static and dynamic friction coefficients are 0.15. Therefore, it can be inferred that in this experimental set-up most of the particle-wall collisions have an impact angle greater than  $27^\circ$ .

Another very interesting observation is the one obtained from analysing the height reached by the particles at stations  $75^\circ$  and  $90^\circ$ . The two first cases are clearly different from the other four. Cases  $F(\mu) = 2$  to  $F(\mu) = 5$  achieve a very similar height at the two latter stations, even though the value of the friction coefficients of each case are distinct. A first guess about the cause of this phenomenon is the type of collision given by the limiting velocity  $v_{lim}$ . Its value is directly proportional to the static friction coefficient  $\mu_{st}$ . Lower values of  $\mu_{st}$  give smaller limiting velocities  $v_{lim}$ , and therefore, there are more collisions behaving as *sliding* and fewer as *non-sliding*. On the other, when higher values of  $\mu_{st}$  are considered, more particle-wall collisions are defined as non-sliding. Anyway, further studies must be carried out to better understand the herein mentioned effect and confirm this hypothesis.

Comparing cases  $F(\mu) = 4$  and  $F(\mu) = 5$  at station  $90^\circ$ , and as already commented by Pereira et al.,<sup>22</sup> it is observed that there are no considerable differences setting a dynamic friction coefficient lower than the static one ( $\mu_{dy} < \mu_{st}$ ). Both cases set the same value for the static friction coefficient although a notably different dynamic friction coefficient. Nonetheless, at stations  $45^\circ$  to  $75^\circ$ , case  $F(\mu) = 5$  behaves as a mixture between cases  $F(\mu) = 2$  (same  $\mu_{dy}$ ) and  $F(\mu) = 4$  (same  $\mu_{st}$ ). That means that some particles tend to impact in certain regions of the bend with lower velocities, presenting *sliding* collisions while other particles tend to collide at higher-velocities, resulting in *non-sliding* collisions. This observation is strongly correlated with the previous one.

## ASSESSMENT OF NUMERICAL ASPECTS USING LES IN PS DEVICES

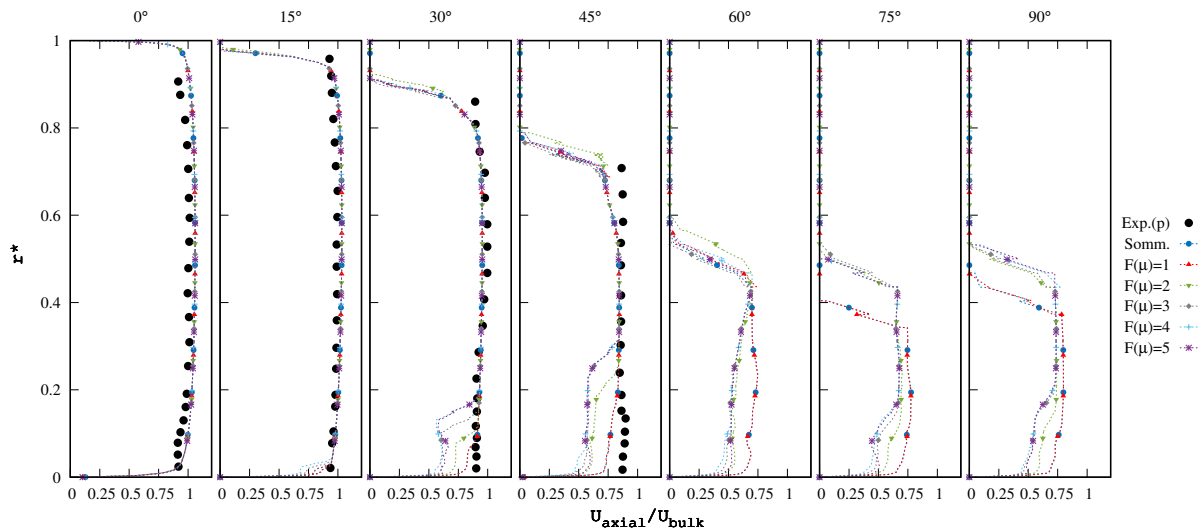


Figure 14: Results comparing different models for evaluating both static ( $\mu_{st}$ ) and dynamic ( $\mu_{dy}$ ) friction coefficients.

## 5. Conclusions

An exhaustive analysis about the influence of different models and numerical aspects on particle-laden flows in the framework of LES modelling has been presented. The study has been done over the benchmark case presented by Kliafas and Holt.<sup>16</sup> Their experimental set-up consisted in a vertical-to-horizontal cross-squared duct with a 90° bend. This configuration is optimum for the detailed study of the relevant physics that plays a key role in IPS. IPS are devices designed for the separation and removal of FOD at the inlet of systems which their operation can be compromised or their useful life severely shortened if certain FOD is ingested by them, e.g., the turbo-compressor of eECS in aircrafts. CFD simulations can help in both design and optimization stages of these devices. Nonetheless, aiming to obtain reliable results from these simulations, the influence and relevance of different numerical aspects must be addressed. Some of these aspects have been studied and assessed in this work. The major findings obtained from these studies can be summarized as:

- Numerical simulations of confined flows using LES modelling are very dependant on the turbulence model employed to close Eq. (2) and model the residual stress tensor ( $\tau^R$ ). It is required a suitable turbulence model able to correctly predict the boundary layers of confined flows in order to obtain accurate predictions of these flows.
- Mesh is a very important aspect and it will affect the accuracy in the results of both phases. Nonetheless, a mesh is not an independent aspect, and considering if a mesh is good enough to obtain reliable and accurate results will depend on the combination between the mesh and the numerical algorithm employed.
- Simulations using LES are very sensitive to the inlet boundary conditions. Therefore, the boundary conditions must be correctly defined.
- From all the forces acting over the dispersed phase, the relevance of each one of them will depend on the characteristics of the studied case, i.e, its physical properties and the associated characteristic time-scales. Therefore, the most relevant forces acting over the particles must be taken into account, while the ones with a negligible effect can be discarded, helping to decrease the computational requirements.
- When simulating dispersed multi-phase flows where particle-wall collisions take place, it must be taken into account that these collision are inelastic and that the surfaces have a certain roughness. Surface roughness must be taken into account using some model. This model should predict how the particle will interact with a surface that is not smooth. This is very relevant since wall-roughness will strongly affect the trajectory of the particles after their collision against the wall. Inelastic collisions can be modelled using a hard sphere collision model accounting for the friction. This model depends on the restitution and friction coefficients ( $e_n$ ,  $e_t$ ,  $\mu_{st}$  and  $\mu_{dy}$ ). The physics of the particle-wall collision are very sensitive to the values of these coefficients. Therefore, their value must be correctly modelled in order to obtain accurate results.

## ASSESSMENT OF NUMERICAL ASPECTS USING LES IN PS DEVICES

Although the studies carried out in this work present some interesting findings, do not answer all the possible questions regarding the influences of certain numerical aspects for confined dispersed multi-phase flows. Therefore, below are detailed some possible interesting future works aiming to complete and extend the analyses done in the present work:

- It would be interesting to assess and study the influence and relevance of the contribution of the sub-grid scales on the dispersed phase. Many numerical studies in LES modelling neglect the effect of the sub-grid velocity over the particles (i.e.,  $\mathbf{u} = \bar{\mathbf{u}}$ ).<sup>1,5</sup> Nonetheless, this assumption may not be valid if there is a medium or high residual energy content in the key regions of the computational domain.
- In the current study it has been considered that particles do not rotate. For the studied configuration it would be interesting to study the effect of accounting for particle rotation and the associated forces like Magnus lift force.
- Another interesting study it would be to analyse if the Saffman lift force becomes more relevant when fully-resolving the shear-layer, i.e., employing mesh E.
- It can be considered to analyse the relevance of the particle-particle interaction. The studied configuration is a very dilute flow, and hence, this phenomena should not play an important role in this case.<sup>7,8</sup> Nonetheless, in more dense flows the collisions between particles can become very relevant.

## 6. Acknowledgements

This work has been developed within the EU H2020 Clean Sky 2 research project “A New proTectIon devIce for FOD - ANTIFOD” (grant agreement N° 821352).

## References

- [1] Sourabh V Apte, Krishnan Mahesh, and Parviz Moin. Large-eddy simulation of evaporating spray in a coaxial combustor. *Proceedings of the Combustion Institute*, 32(2):2247–2256, 2009.
- [2] A. B. Basset. On the motion of a sphere in a viscous liquid. *Philosophical Transactions of the Royal Society of London A: Mathematical, Physical and Engineering Sciences*, 179:43–63, 1888.
- [3] Joseph Boussinesq. Sur la résistance qu’oppose un liquide indéfini en repos. *CR Acad. Sci. Paris*, 100:935–937, 1885.
- [4] M Breuer, M Alletto, and F Langfeldt. Sandgrain roughness model for rough walls within eulerian–lagrangian predictions of turbulent flows. *International Journal of Multiphase Flow*, 43:157–175, 2012.
- [5] M. Chrigui, J. Gounder, A. Sadiki, A.R. Masri, and J. Janicka. Large Eddy Simulation of a Polydisperse Ethanol Spray Flame. 90:813–832, 2013.
- [6] Clayton T. Crowe, John D. Schwarzkopf, Martin Sommerfeld, and Yutaka Tsuji. *Multiphase flows with droplets and particles*. CRC press, 2011.
- [7] S Elghobashi. On predicting particle-laden turbulent flows. *Applied scientific research*, 52(4):309–329, 1994.
- [8] Said Elghobashi. An updated classification map of particle-laden turbulent flows. *Fluid Mechanics and Its Applications*, 81:3, 2006.
- [9] Antonio Filippone and Nicholas Bojdo. Turboshift engine air particle separation. *Progress in Aerospace Sciences*, 46(5-6):224–245, 2010.
- [10] Swedish Industrial Association for Multiphase Flows (SIAMUF) and Martin Sommerfeld. *Best Practice Guidelines for Computational Fluid Dynamics of Dispersed Multi-Phase Flows*. European Research Community on Flow, Turbulence and Combustion (ERCOFTAC), 2008.
- [11] Alister Forder, Martin Thew, and David Harrison. A numerical investigation of solid particle erosion experienced within oilfield control valves. *Wear*, 216(2):184 – 193, 1998.

- [12] G. Grant and Widen Tabakoff. Erosion prediction in turbomachinery resulting from environmental solid particles. *Journal of Aircraft*, 12(5):471–478, 1975.
- [13] Thomas J.R. Hughes, Luca Mazzei, and Kenneth E. Jansen. Large eddy simulation and the variational multiscale method. *Computing and Visualization in Science*, 3(1):47–59, May 2000.
- [14] J. Kim and P. Moin. Application of a fractional-step method to incompressible Navier-Stokes equations. *Journal of Computational Physics*, 59(2):308–323, 1985.
- [15] M Klein, A Sadiki, and J Janicka. A digital filter based generation of inflow data for spatially developing direct numerical or large eddy simulations. *Journal of computational Physics*, 186(2):652–665, 2003.
- [16] Y. Kliafas and M. Holt. LDV measurements of a turbulent air-solid two-phase flow in a 90° bend. *Experiments in Fluids*, 5(2):73–85, Mar 1987.
- [17] O. Lehmkuhl, C.D. Pérez Segarra, R. Borrell, M. Soria, and A. Oliva. Termofluids: A new Parallel unstructured CFD code for the simulation of turbulent industrial problems on low cost PC cluster. pages 1–8, 2007.
- [18] M. R. Maxey and J. J. Riley. Equation of motion for a small rigid sphere in a nonuniform flow. *Physics of Fluids*, 26:883–889, April 1983.
- [19] Renwei Mei. An approximate expression for the shear lift force on a spherical particle at finite reynolds number. *International Journal of Multiphase Flow*, 18(1):145–147, 1992.
- [20] Franck Nicoud and Frédéric Ducros. Subgrid-scale stress modelling based on the square of the velocity gradient tensor. *Flow, turbulence and Combustion*, 62(3):183–200, 1999.
- [21] Carl Wilhelm Oseen. Hydrodynamik. *Akademische Verlag, Leipzig*, 1927.
- [22] Gabriel Chucru Pereira, Francisco José de Souza, and Diego Alves de Moro Martins. Numerical prediction of the erosion due to particles in elbows. *Powder Technology*, 261:105–117, 2014.
- [23] Stephen B Pope. *Turbulent flows*. Cambridge Univ. Press, Cambridge, 2011.
- [24] P. Sagaut. *Large Eddy Simulation for Incompressible Flows: An Introduction*. Scientific Computation. Springer, 2006.
- [25] Bulent Sarlioglu and Casey T Morris. More electric aircraft: Review, challenges, and opportunities for commercial transport aircraft. *IEEE transactions on Transportation Electrification*, 1(1):54–64, 2015.
- [26] L. Schiller and Z. Naumann. A drag coefficient correlation. *Z. Ver. Deutsch. Ing.*, 77(1):318–320, 1935.
- [27] R.K. Shah, A.L. London, T.F. Irvine, and J.P. Hartnett. *Laminar Flow Forced Convection in Ducts: A Source Book for Compact Heat Exchanger Analytical Data*. Elsevier Science, 2014.
- [28] Mike Sinnett. 787 no-bleed systems: saving fuel and enhancing operational efficiencies. *Aero Quarterly*, 18:6–11, 2007.
- [29] Joseph Smagorinsky. General circulation experiments with the primitive equations: I. The basic experiment. *Monthly weather review*, 91(3):99–164, 1963.
- [30] M. Sommerfeld and N. Huber. Experimental analysis and modelling of particle-wall collisions. *International journal of multiphase flow*, 25(6-7):1457–1489, 1999.
- [31] Shankar Subramaniam. Lagrangian-Eulerian methods for multiphase flows. *Progress in Energy and Combustion Science*, 39(2):215–245, 2013.
- [32] F.X. Trias and O. Lehmkuhl. A Self-Adaptive Strategy for the Time Integration of Navier-Stokes Equations. 60(2):1116–134, 2011.
- [33] R.W.C.P. Verstappen and A.E.P. Veldman. Symmetry-preserving discretization of turbulent flow. 187:343–368, 2003.